NASA Technical Memorandum 104362

Simulation of Iced Wing Aerodynamics

M.G. Potapczuk
Lewis Research Center
Cleveland, Ohio

M.B. Bragg
University of Illinois at Urbana–Champaign
Urbana, Illinois

O.J. Kwon and L.N. Sankar
Georgia Institute of Technology
Atlanta, Georgia

NASA

Simulation of Iced Wing Aerodynamics

M.G. Potapczuk
NASA Lewis Research Center
Cleveland, Ohio 44135
M.B. Bragg
University of Illinois at Urbana-Champaign
Urbana, Illinois 61801
O.J. Kwon
L.N. Sankar
Georgia Institute of Technology
Atlanta, Georgia 30332

Summary

The sectional and total aerodynamic load characteristics of moderate aspect ratio wings with and without simulated glaze leading-edge ice are studied both computationally, using a three-dimensional, compressible Navier-Stokes solver, and experimentally. The wing has an untwisted, untapered planform shape with NACA 0012 airfoil section. The wing has an unswept and swept configuration with aspect ratios of 4.06 and 5.0, respectively. Comparisons of computed surface pressures and sectional loads with experimental data for identical configurations are given. The abrupt decrease in stall angle of attack for the wing, as a result of the leading edge ice formation, is demonstrated numerically and experimentally.

List of Symbols

b	span length at leading edge
C_l	sectional lift coefficient
C_L	wing lift coefficient
C_p	pressure coefficient
F,F	inviscid flux vector
G,G	inviscid flux vector
H,H	inviscid flux vector
q,q	flow properties vector
R,R	viscous terms
S,S	viscous terms
T,T	viscous terms
t	time
x	Cartesian coordinate
y	Cartesian coordinate
y	spanwise coordinate
z	Cartesian coordinate
η	curvilinear coordinate
t	time
ξ	curvilinear coordinate
ζ	curvilinear coordinate

1. Introduction

The adverse effects of ice formation on the aerodynamic characteristics of wings and helicopter blades are well known.[1,2] It is known that icing may cause premature flow separation and lead to stall at angles of attack as low as 6 degrees. Techniques for quantitative prediction of the 3D leading edge ice formation process and the effects of icing on the aerodynamic performance of wings and rotors are however not well developed. Reliable techniques for quantitative prediction of the above phenomena are urgently needed, so that next generation aircraft and rotorcraft may be designed to cope with icing. Additionally, experimental iced wing flow field data is required for code validation efforts.

Recognizing the need for improved understanding of the aircraft icing phenomena, a multi-disciplinary research program has been underway under the funding and direction of NASA Lewis Research Center, for the past several years. Work performed under this program covers areas such as:

- Numerical modeling of the ice accretion process and development of an associated code validation database

- Experimental studies of the effects of icing on the aerodynamic characteristics of finite wings

- Efficient engineering tools based on a combination of panel methods and interactive boundary layer schemes to predict aerodynamic characteristics up to stall onset

- Research tools based on 3D Navier-Stokes equations to study the pre- and post stall characteristics of finite wings

These activities, although only a portion of the overall icing effort, constitute a major part of the program for simulation of an icing encounter for a fixed wing aircraft.

Initial research on development of analytical and computational tools for simulation of iced airfoil aerodynamics was centered on two-dimensional flows.[3-5] This was supported by an extensive experimental program for characterization of the 2D iced airfoil flow field.[6-8] Results of that research indicated reasonable agreement between code and experiment for angle of attack conditions up to stall. There is still some concern over the role of turbulence models in the prediction of massive separation at stall condition.[4,9]

The present work describes the NASA sponsored effort to develop a validated 3D Navier-Stokes solver for study of the aerodynamic characteristics of isolated wing configurations for non-iced and iced conditions. The computer code was developed by Sankar, et al.[10-12] and the current calculations were performed by Kwon and Sankar.[13,14] The experimental results were produced by Bragg and his students.[8,15,16] The wing geometry being considered has an untwisted, untapered planform shape with NACA 0012 airfoil section. The wing has an unswept and swept configuration with aspect ratios of 4.06 and 5.0, respectively.

The results presented have been documented in previous publications.[8,13-16] However, this paper provides an opportunity to assess the current status of the simulation effort for iced aircraft aerodynamics, to discuss the issues as yet unresolved, and to suggest the direction for future research. Detailed comparisons with experiments of the surface pressures and sectional airloads are used to provide a basis for the discussion.

2. Code Description

2.1 Governing Equations

The equations governing unsteady three-dimensional flow are the full Navier-Stokes equations, and may be written in a Cartesian coordinate system as:

$$q_t + F_x + G_y + H_z = R_x + S_y + T_z \qquad (1)$$

Here, q is the unknown flow properties vector; F, G and H are the inviscid flux vectors; R, S, and T are the viscous terms. To facilitate treatment of arbitrary planforms and airfoil shapes, the equations are solved in a body-fitted coordinate system. The following general curvilinear coordinate system is used:

$$\xi = \xi(x,y,z,t) \qquad \eta = \eta(x,y,z,t)$$
$$\qquad (2)$$
$$\zeta = \zeta(x,y,z,t) \qquad \tau = t$$

In such a coordinate system, the governing equations may be written in the following strong conservation form:

$$q_\tau + F_\xi + G_\eta + H_\zeta = R_\xi + S_\eta + T_\zeta \qquad (3)$$

The quantities q, F, G, H, R, S, T are related to their Cartesian counterparts through the metrics of transformation. For a detailed description of the flow and flux vectors in the Cartesian and transformed coordinate systems, the reader is referred to Reference 12.

A two layer Baldwin-Lomax eddy viscosity model patterned after the well known Cebeci-Smith model has been used in this work. Use of such a simple model in massively separated flows may be considered questionable. In order to address this concern, studies of 2D stalled flows for iced airfoils using other models have been conducted by Potapczuk[4,9] and Wu.[17] Potapczuk used a modified mixing length model and found some improvement in the simulation for conditions at stall, however those results require further investigation for 3D calculations. Wu's results indicate that the use of higher order turbulence models does not significantly improve the accuracy of the simulation for iced airfoils. In order to keep the computer time resources small, the Baldwin-Lomax model has been used in all the 3D calculations presented here.

2.2 Solution Procedure

The governing equations are parabolic in time, and may be advanced in time using a suitable stable, dissipative scheme. Standard second-order accurate, central differences are used to approximate the spatial derivatives and to compute the metrics of the transformation. The flux vectors F and H are linearized while the spanwise flux vector, G, is treated semi-implicitly, thus requiring no time linearization. The viscous terms are treated explicitly. The time derivative is approximated as a first-order accurate, two-point backward difference.

2.3 Grid Generator

An algebraic C-grid generator has been built in to the computer code, and can generate computational grids around arbitrary planforms and arbitrary airfoil sections. The grid generation methodology is based on the sheared parabolic coordinate scheme. The user needs to prescribe the leading edge coordinates and the section chord and twist at chosen stations. The grid generation routines perform the necessary interpolation (linear along the span and cubic in the chordwise direction) to enrich the input wing shape. After the sheared parabolic grid is generated, the points along the grid lines in the direction approximately normal to the wing surface are redistributed so that, the first point off the wall is at a user specified distance off the surface, and an adequate number of points are placed within the boundary layer. A typical grid for a swept wing is presented in Figure 1 which shows the upper half of the computational domain at the

wing root plane and on the surface of the wing. The grid at the wing root plane can be used as a reflection plane or as a solid surface representing the wind tunnel wall.

2.4 Boundary Conditions

In the present numerical procedure, all the boundary conditions are applied explicitly after each time step. Since these cases deal with low subsonic Mach numbers, the flow quantities at the far-field are set to be the undisturbed freestream conditions. To satisfy this condition, the far-field boundaries are placed at least 6 to 7 chord lengths from the surface of the wing. At the downstream boundary, the pressure is assumed to recover to freestream values and all the other flow properties are extrapolated from the interior. The C-grid generated by the present algebraic transformation created a cut that originates from the trailing edge. On this cut the flow quantities are averaged from above and below.

Two types of boundary conditions have been used at the wing root location. The experimental model is a semi-span wing with a splitter wall at the root location. This splitter wall is used to minimize the effects of the tunnel wall boundary layer on the flow over the wing. The wing-splitter wall intersection results in the development of a vortical flow region which reduces the effective angle of attack at the wing root. This effect is minor for the non-iced geometry but can play an important role in the aerodynamics of the iced wing. In order to properly capture this phenomena, a no-slip boundary condition is applied at the wing root-splitter plate junction for the iced geometry. The spanwise spacing of nodal planes in this region is quite small in order to capture these effects, thus resulting in a significant increase in the number of grid points to be computed. In the case of a non-iced geometry, a reflection plane was used at the root, thus allowing coarser grid spacing in the spanwise direction and hence a less costly computation.

3. Description of Experiment

3.1 Apparatus

The experiments described in this report were conducted in the Ohio State University (OSU) subsonic wind tunnel located at the Aeronautical and Astronautical Research Laboratory and later in the subsonic wind tunnel at the University of Illinois. The OSU tunnel has a three-by-five foot test section, eight feet in length. The tunnel operates at speeds from zero to 200 feet per second at Reynolds numbers of up to 1.3×10^6 per foot. The tunnel is an open return type and uses four turbulence screens and honeycomb in the settling chamber to reduce tunnel turbulence. The University of Illinois tunnel is of similar design with a three-by-four foot test section, eight feet in length. The Illinois tunnel operates at speeds

from zero to 240 feet per second at Reynolds numbers of up to 1.5×10^6 per foot.

The model used in testing is a semi-span wing having a NACA 0012 airfoil section with a variable (i.e. $0°$ or $30°$) sweep angle. Results have been obtained using both sweep angles. The model has a chord of 15 inches perpendicular to the leading edge and a span of 35.18 inches. The chord length was chosen to provide as large an aspect ratio as possible with minimum tunnel wall interference and high Reynolds number. The model has a removable leading edge, thus allowing simulation of a non-iced or iced wing geometry. The iced leading edge is a simulation of a measured ice accretion on a NACA 0012 airfoil taken from the NASA Lewis Icing Research Tunnel. A cross-sectional view of the simulated glaze ice shape is shown in Figure 2.

The model is equipped with surface static pressure taps, as shown in Figure 3. The taps are located in 5 major rows plus a row on the tip section. Only the 5 major pressure tap rows are shown in the figure, as they were the ones used for comparison to the computations. The centerline row of taps has 80 taps in the no-ice configuration and 83 in the iced configuration. The other 4 rows on the main element have 40 and 41 taps in the no-ice and iced configurations, respectively. The wing tip section has 21 taps. The total number of pressure taps on the model is thus, 261 in the no-ice configuration and 268 in the iced configuration.

Pressure measurements were made using a Scanivalve system. Six Scanivalves capable of measuring 48 pressures each were used. No cut-off valves were used during the testing. For the zero-sweep tests, a single traversing total-pressure probe was used to measure the airfoil wake. The probe was located approximately one chord length downstream of the model trailing edge and at the spanwise station, $y/b = 0.417$, which is between the second and third tap rows.

3.2 Pressure Data Reduction

The model pressures were converted to pressure coefficients using the measured tunnel dynamic pressure taken from each of the Scanivalves. The pressure coefficients were integrated over the surface of the model to produce the section lift coefficient. The total pressure deficit, measured by a wake probe, was integrated to obtain the airfoil section drag for the zero sweep model. Note that when span loads are shown, y is taken parallel to the leading edge and C_l is taken along the tap lines perpendicular to the leading edge. When the span loads are integrated to obtain model C_L, the sectional lift coefficient at the wing root is taken as equal to value for the first tap row and the C_l at the tip is approximated as 1/2 that of the last tap row.

Further details regarding the equipment used for data acquisition and reduction are provided in References 6-8, 15, and 16.

3.3 Helium -Bubble Flow Visualization

Helium-bubble flow visualization was conducted using a bubble generator manufactured by Sage Action, Inc. The bubbles are approximately 1/16 inch in diameter and are formed by injecting helium into a special soap film using a concentric injection tube arrangement.[18] The helium-filled bubbles are approximately neutrally buoyant and are able to follow the complex separated flows found on iced airfoils. Two bubble generator heads producing a total of 800 bubbles per second were located in the tunnel settling chamber just aft of the turbulence screens.

The bubbles are illuminated from a point orthogonal to the viewing position. For the planform or top view shown later in this paper, the light beam entered the tunnel through the side window, over the wing tip. Photos. were then taken through a plexiglass window in the tunnel floor and the model was mounted inverted, upper surface down.

Details regarding the photographic equipment and video recording equipment used to capture the bubble images are contained in Reference 16.

4. Results and Discussion

The experiments and computations were carried out for a combination of conditions encompassing the iced and non-iced geometry, the $0°$ and $30°$ sweep angles, and $4°$ and $8°$ angle of attack conditions. This discussion will center on a review of progress to date, issues that remain unresolved, and on what activities are planned to address those issues.

4.1 Rectangular Wing

The pressure distributions at several spanwise locations for the non-iced unswept wing at the $8°$ angle of attack condition are shown in Figure 4. These results show very good agreement at all the span locations. The pressure peaks near the leading edge are captured quite well. Some differences are seen near the trailing edge region, most likely due to poor grid resolution. The profile at the 85 percent span location indicates an overprediction of the C_p values by approximately 5 percent for the first 20 percent chord.

The effect of the wall boundary condition is also seen in Figure 4. The differences in C_p due to the wall, at the measurement locations, is not large. However, differences are apparent when the calculated results using either set of wall boundary conditions are compared at locations inboard of the 17 percent span location. Figure

5 shows these differences. The wall boundary condition actually increases the lift. No measurements have been taken in this region, however the effects of the splitter-wall boundary layer will be investigated in future testing through the use of a side-wall suction mechanism.

Figure 6 shows the spanwise distribution of the computed and measured airloads (i.e. measured surface pressures integrated over the chord) at $4°$ and $8°$ angle of attack for a non-iced unswept wing. The computed airloads are generally in good agreement with the measured loads over the span, even though the rate of decrease along the span between the mid semi-span and the tip is smaller than in the experiment. This gives slightly higher loading in this range. These discrepancies are partly attributable to the lack of spanwise grid points which are necessary to properly handle the concentrated vortex shedding off the wing tip.

The addition of the ice shape to the leading edge causes a considerable change to the surface pressure distributions. The recirculation region behind the ice shape alters the pressure peaks at the leading edge. The typical flat profile of a separated flow region is indicated by the experimental results for the $4°$ angle of attack condition, as seen in Figure 7. The calculated results, also shown in Figure 7, indicate a much larger pressure spike at the leading edge than the experiments suggest. This phenomenon has been seen by other researchers[4,5] and has yet to be examined in detail. It has been suggested that this may be due coarse grid code resolution around the ice horn. The spanwise distribution of the computed and measured airloads are shown in Figure 8. The results indicate very good agreement for the $4°$ angle of attack condition.

At $8°$ angle of attack, the importance of the wall boundary condition becomes apparent. Figures 9 and 10, C_p distributions at several spanwise locations, show the results of using the no-wall and wall boundary conditions, respectively. It is suggested that the interaction of the separation region behind the ice shape with the wing-wall vortex at the root leads to reattachment of the separated flow. Neglecting this interaction, as in the calculations for Figure 9, results in separation over the entire length of the wing at the root sections and underprediction of the C_p suction peak. The spanwise load distributions (Figure 8) also show the influence of the wall boundary condition on the computed results.

The grid required to incorporate the wall boundary conditions consisted of a 151 by 42 by 43 array of nodal points. Obviously, this is a significant increase in the computational requirements of the calculation when compared to the no-wall calculation, which has a 131 by 19 by 30 array of nodal points. This doubling of the size of the grid is necessary in this case because the no-wall

boundary condition misses a significant part of the physics of this problem.

The other point to be made here is that the wall boundary condition must be included in all calculations, if the code is to be used as a predictive tool. Since it is not known beforehand at what angle of attack the recirculation zone will develop into a completely separated region, the wall boundary condition must be used to insure that the code does not prematurely predict separation and stall of the iced wing. This also suggests that two-dimensional calculations for the stall of an iced wing will undoubtedly result in conservative predictions for the performance behavior.

4.2 Swept Wing

The effect of sweep on the wing model is seen in Figure 11 which shows the integrated lift values for positive and negative angles of attack, as measured in the wind tunnel. The swept wing has a lower lift-curve slope and a higher stall angle than the rectangular wing model.

The influence of the wall boundary condition is seen in Figures 12 and 13, which show C_p distributions and spanwise lift distributions, respectively. Both figures indicate that the wall does not significantly influence the aerodynamics of the non-iced swept wing.

The pressure distributions at several spanwise locations for the 4° angle of attack condition are shown in Figure 14. The comparisons to experiment indicate good agreement except for the pressure spike at the horn of the ice shape and the oscillation in the pressure trace at the trailing edge. As mentioned in the discussion of results for the rectangular wing, the leading edge pressure spike has been attributed to lack of resolution in the computations,[4,5,13] although no attempt has been made to systematically verify that contention. A similar argument is made for the evaluation of the trailing edge region. The large number of grid points needed to characterize the iced wing geometry has led to some compromise on accuracy of the solution in non-critical regions. This compromise has not resulted in poor agreement between computation and experiment for the airloads, as seen in Figure 15.

Particle traces developed from the calculated results are shown in Figures 16 and 17. The figures indicate a separation zone near the leading edge of the wing covering most of the span. Figure 16, a surface oil flow simulation, indicates the reattachment line at 10 percent chord and the spanwise flow from root to tip. Figure 17, consisting of particle traces ranging from zero to one chord length above the wing surface, shows the vortical nature of the flow in the separation zone. This figure can be compared to the photograph of a helium bubble flow visualization experiment, conducted in the Univ. of Illinois wind tunnel, shown in Figure 18. The photograph

also shows the vortical flow in the separation zone, albeit with fewer traces due to the random nature of the bubble entrainment process.

The 8° angle of attack results indicate the onset of stall for the wing, progressing from the tip towards the root. The pressure distribution comparisons, Figure 19, show regions of increasing flow separation moving from the root to the tip. The comparisons between the calculated results and the measurements are quite good, even at the outboard stations. The spanwise load distributions, shown in Figure 15, are also in good agreement. The code appears to be capable of indicating the onset of stall for the iced wing.

Figures 20 and 21 are particle traces from the calculated results, as was described for the 4° angle of attack case. The surface oil flow simulation, Figure 20, indicates a much larger region of flow separation. The reattachment line starts at the leading edge near the root and moves toward the trailing edge near the wing tip. At the tip region, the flow separation due to the ice shape merges with the wing tip vortex, thus producing the complex flow pattern seen in the figure. The off-body particle traces, Figure 21, show the center of the vortical flow moving back along the chord as it progresses from the root to the tip. Interaction with the tip vortex causes the center to curve towards the trailing edge very rapidly over the last 30 percent of span. This can also be seen in the change in slope of the lift distribution curve (Fig. 15). Flow visualization experiments are underway in order to verify the existence of the flow patterns seen in the computations.

5. Concluding Remarks

A three-dimensional Navier-Stokes solver has been used to study the performance of non-iced wings and wings with simulated glaze leading-edge ice at 4° and 8° angles of attack. A corresponding wind tunnel test program is underway to provide highly detailed code validation information. The calculated chordwise pressure distribution and the integrated sectional loads of non-iced wings and iced wing at 4° angle of attack are in good agreement with experiments. The locally separated flow region at the iced wing leading edge is reasonably well predicted. At 8° angle of attack, the flow over the iced wing is massively separated. Accurate prediction of chordwise pressure distribution and sectional loads under these conditions requires representation of the tunnel end wall boundary condition due to the highly 3D nature of the flow field.

These results indicate the need for further investigation of the flowfield characteristics of the iced swept wing. Detailed measurements of the velocities above the wing surface are required to validate the computational

6

predictions of the vortical spanwise flow. These measurements will also confirm the changes in flow structure seen as the angle of attack increases. Current plans call for the use of a laser-doppler velocimeter system to obtain the detailed flow measurements required for validation. This system should also provide information on turbulence levels in the flow which will add further to the evidence for validation of the computations. Additionally, a force balance system is being developed to provide integrated lift, drag, and moment measurements for the wing model. Flow visualization experiments will be continued to provide qualitative assessment of the correspondence between calculation and experiment.

On the computational side, more cases must be run to address some of the issues identified above. Grid resolution near the leading and trailing edge regions must be increased to provide better agreement for the pressure distribution on the wing. The grid resolution near the wall region should also be investigated with the goal of decreasing the number of spanwise stations necessary . while maintaining accurate reproduction of the flowfield in that region.

References

1) Preston, G. M. and Blackman, C. C., "Effects of Ice Formations on Airplane Performance in Level Cruising Flight," NACA TN-1598, May 1948.

2) Korkan, K. D., Dadone, L., and Shaw, R. J., "Performance Degradation of Helicopters due to Icing -- A Review," Presented at the 41st Annual Forum of the American Helicopter Society, Ft. Worth, Texas, May 15-17, 1985.

3) Potapczuk, M. G., "Numerical Analysis of a NACA 0012 Airfoil with Leading Edge Ice Accretions," AIAA Paper 87-0101, Jan. 1987.

4) Potapczuk, M. G., "Navier-Stokes Analysis of Airfoils with Leading Edge Ice Accretions," Ph.D. Dissertation, The University of Akron, Akron, OH, 1989.

5) Cebeci, T., "Effects of Environmentally Imposed Roughness on Airfoil Performance," NASA CR-179639, June 1987.

6) Bragg, M. B. and Spring, S. A., "An Experimental Study of the Flow Field about an Airfoil with Glaze Ice," AIAA Paper 87-0100, Jan. 1987.

7) Bragg, M. B. and Khodadoust, A., "Experimental Measurements in a Large Separation Bubble due to a Simulated Glaze Ice Accretion," AIAA Paper 88-0116, Jan. 1988.

8) Bragg, M. B. and Khodadoust, A., "Effect of Simulated Glaze Ice on a Rectangular Wing," AIAA Paper 89-0750, Jan. 1989.

9) Zaman, K.B.M.Q. and Potapczuk, M.G., "The Low Frequency Oscillation in the Flow over a NACA 0012 Airfoil with an "Iced" Leading Edge," NASA TM-102018, June 1989.

10) Sankar, L. N., Malone, J. B., and Schuster, D., "Euler Solutions for Transonic Flow past a Fighter Wing," Journal of Aircraft, Vol. 24, No. 1, Jan. 1987.

11) Sankar, L. N., Wake, B. E., and Lekoudis, S. G., "Solution of the Unsteady Euler Equations for Fixed and Rotary-Wing Configurations," Journal of Aircraft, Vol. 23, No. 4, April 1986.

12) Wake, B. E. and Sankar, L. N., "Solution of the Navier-Stokes Equations for the Flow About a Rotor Blade," Journal of the American Helicopter Society, Vol. 34, No. 2, April 1989.

13) Kwon, O. and Sankar, L., "Numerical Study of the Effect of Icing on Finite Wing Aerodynamics," AIAA Paper 90-0757, Jan. 1990.

14) Kwon, O.J. and Sankar, L.N, "Numerical Study of the Effect of Icing on Fixed and Rotary Wing Performance," AIAA Paper 91-0662, Jan. 1991.

15) Khodadoust, A. and Bragg, M. B., "Measured Aerodynamic Performance of a Swept Wing with a Simulated Ice Accretion," AIAA Paper 90-0490, Jan. 1990.

16) Bragg, M. B., Khodadoust, A.,Soltani, R., Wells, S., and Kerho, M.,"Effect of Simulated Ice Accretion on the Aerodynamics of a Swept Wing," AIAA Paper 91-0442, Jan. 1991.

17) Wu, J.C., "A Study of Unsteady Turbulent Flow Past Airfoils," Ph.D. Dissertation, Georgia Institute of Technology, Atlanta, GA, 1988.

Acknowledgment

7

The computations were performed by O.J. Kwon and L.N. Sankar of the Georgia Institute of Technology on the NASA Lewis Research Center CRAY-YMP.

Fig. 1 Grid system for iced wing with 30° sweep angle. Grid : 151x42x43.
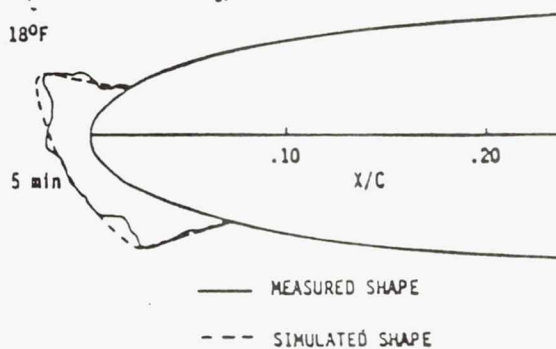
Fig. 2 Simulated glaze ice accretion.
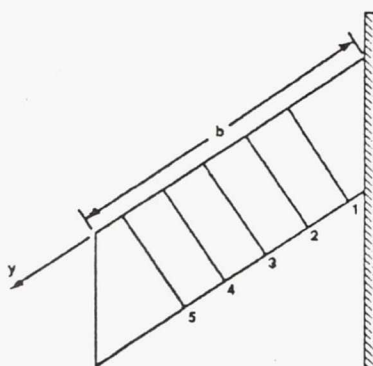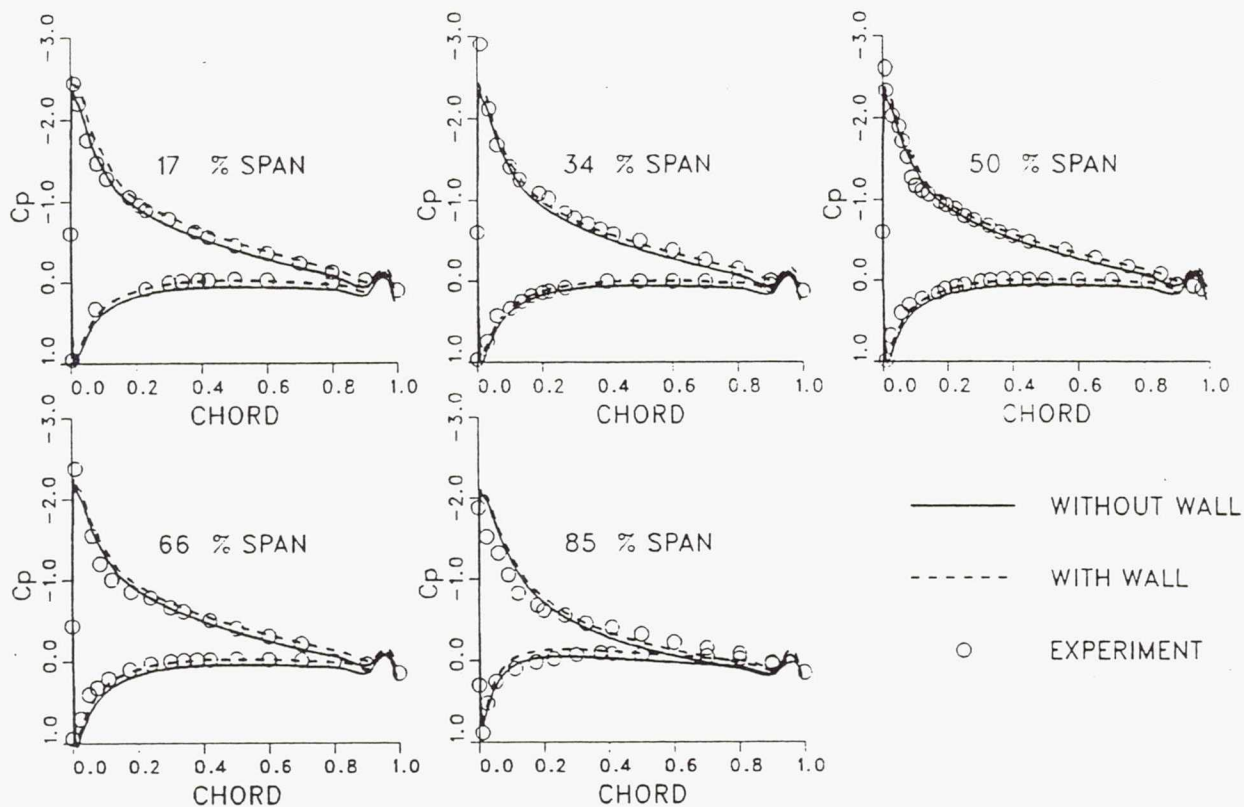

Fig. 3 Semi-span swept wing model including pressure tap locations.

Fig. 4 Surface pressure distributions for the non-iced unswept wing at 8° angle of attack. Wall and no-wall boundary at root section.
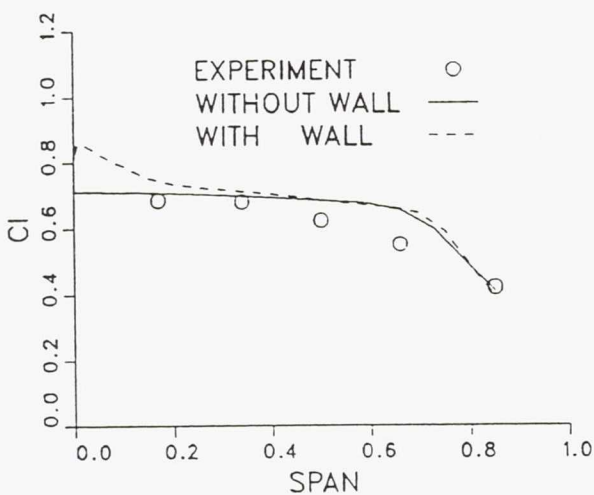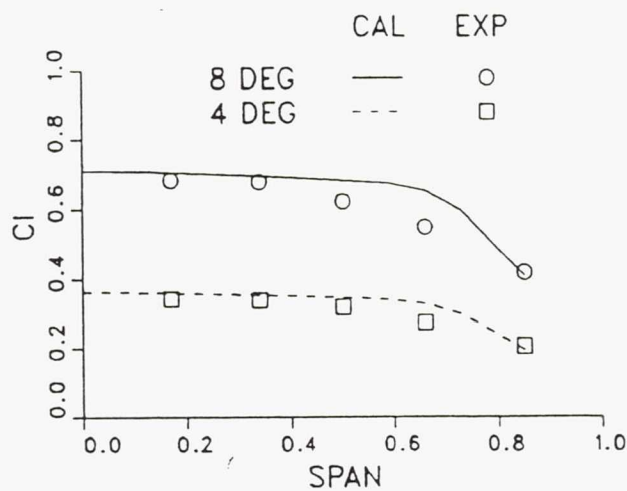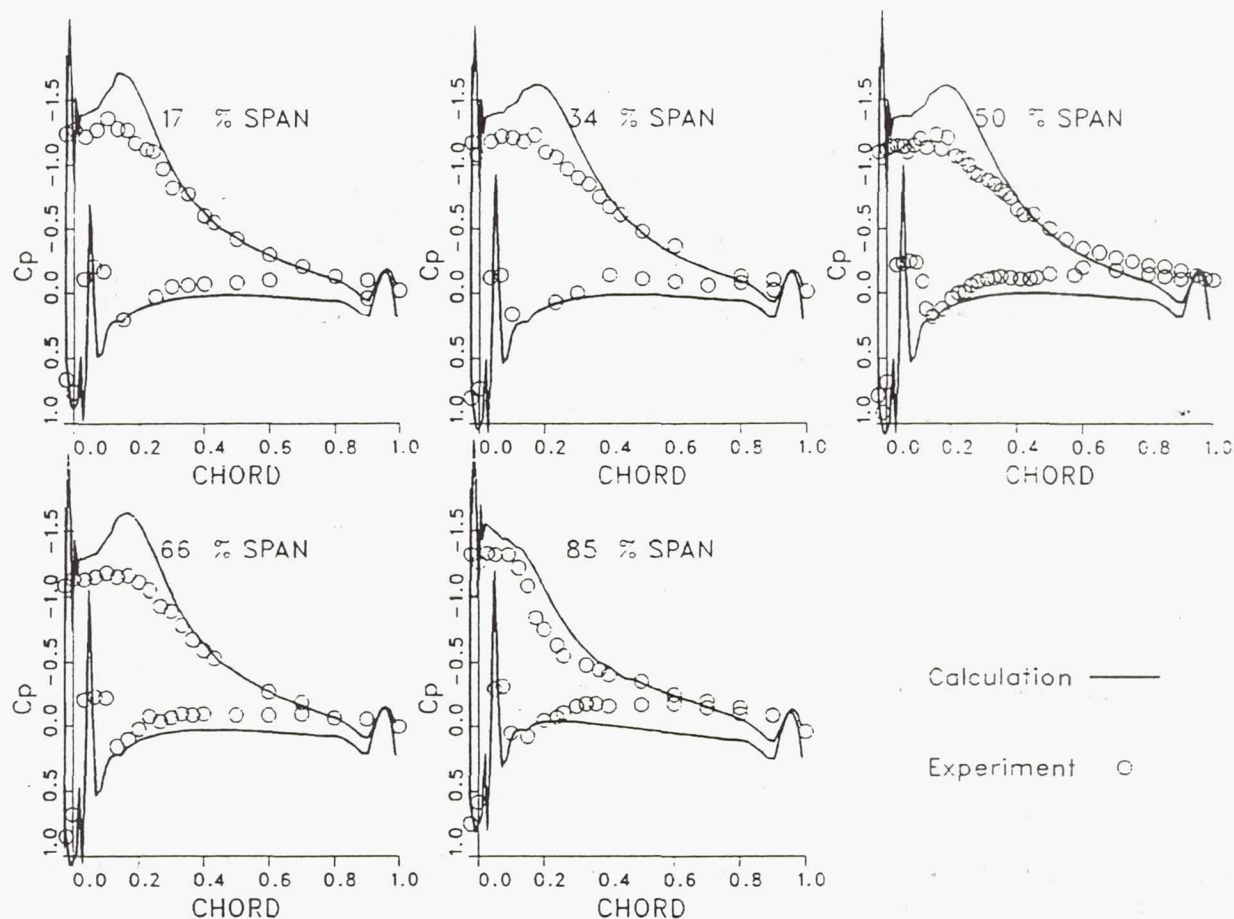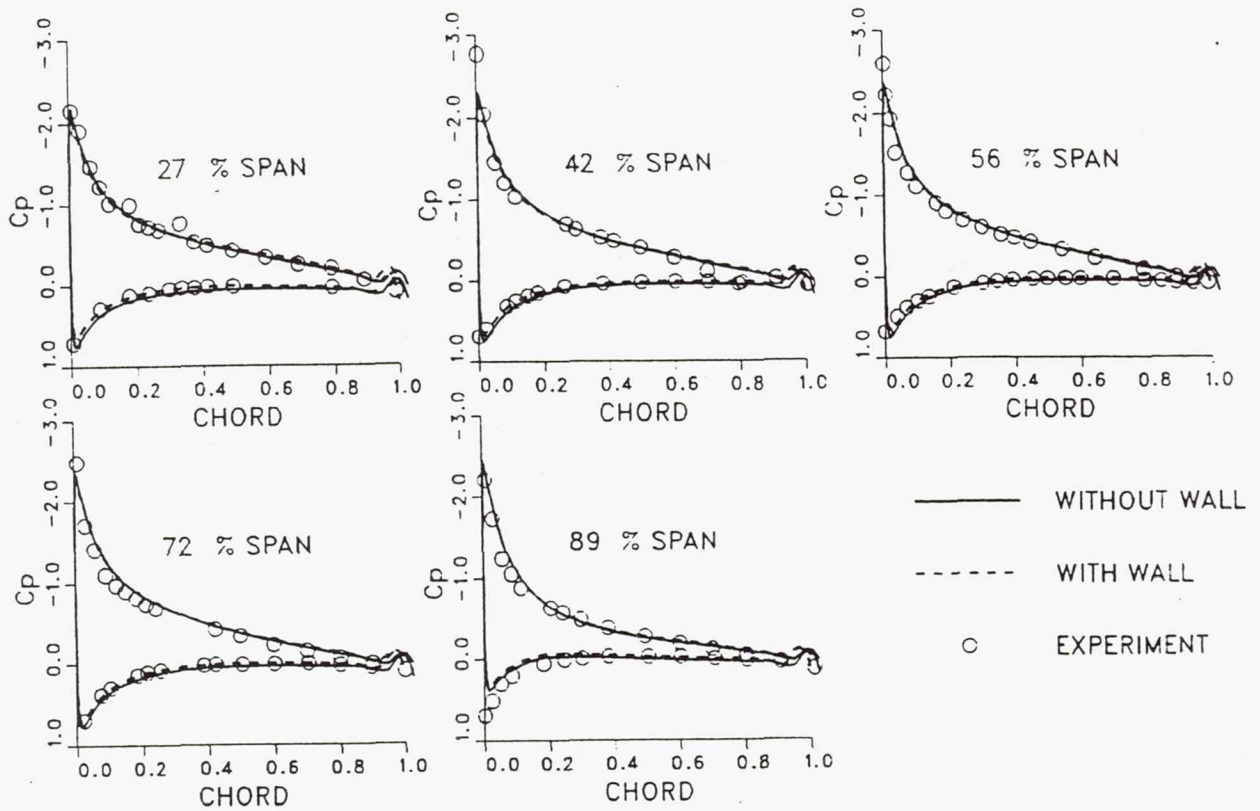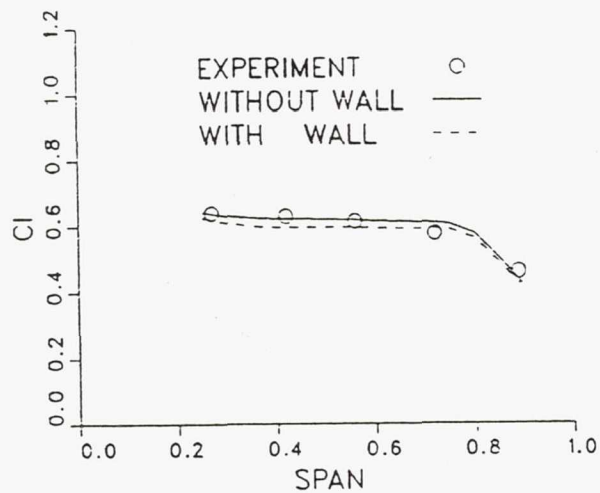
Fig. 5 Spanwise load distributions for the non-iced unswept wing at 8° angle of attack. Wall and no-wall boundary at root section.
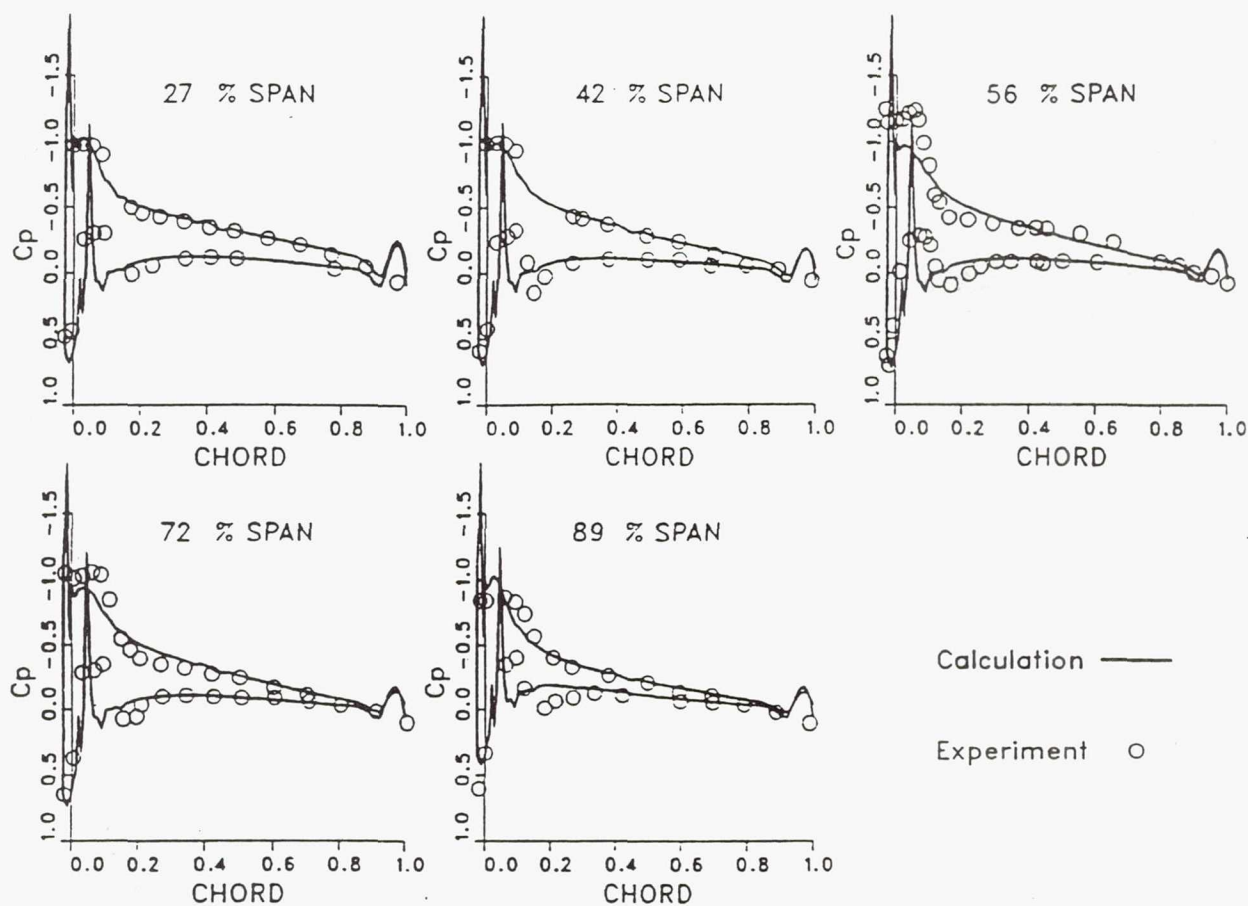
Fig. 6 Spanwise load distributions for the non-iced unswept wing at 4° and 8° angle of attack.
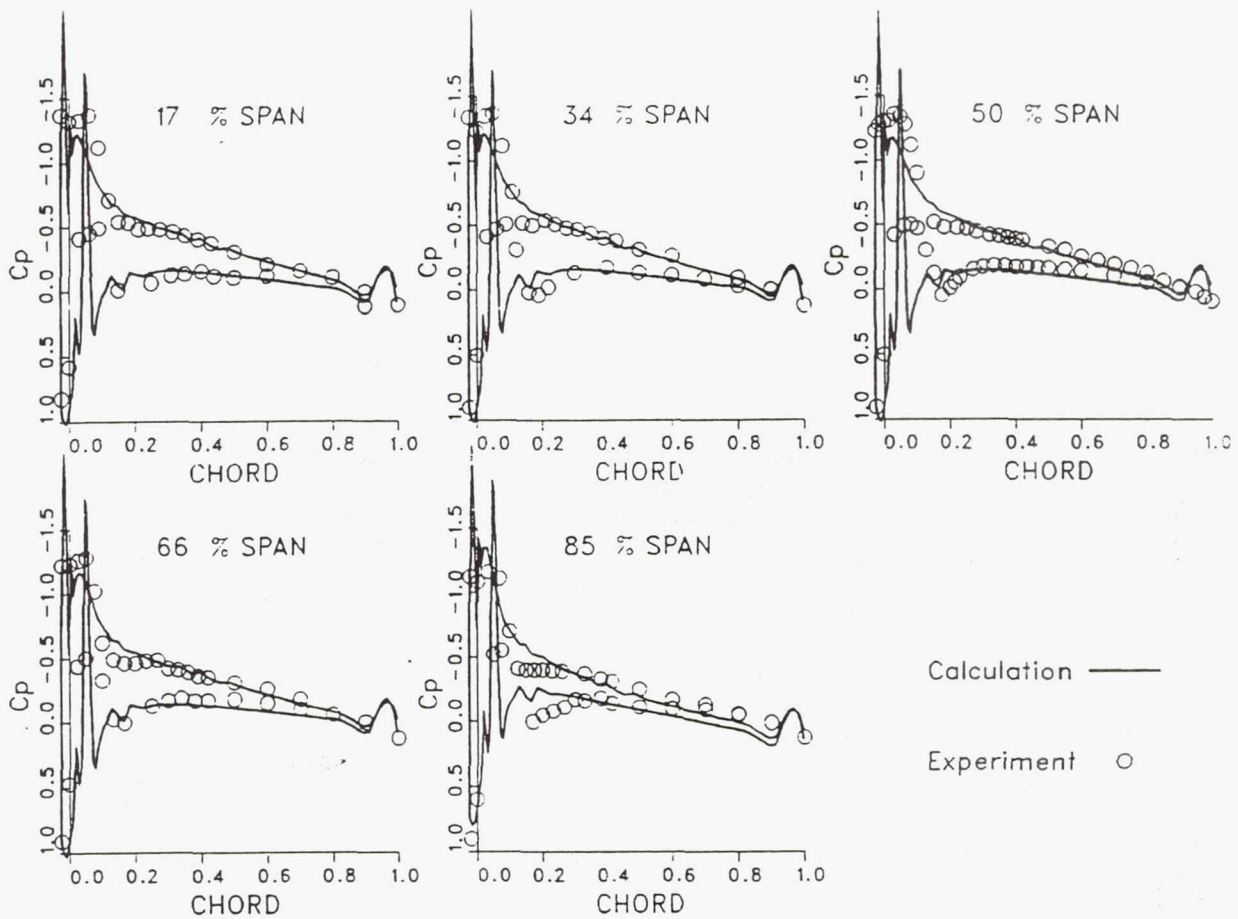
Fig. 7 Surface pressure distributions for the iced unswept wing at 4° angle of attack. No-wall boundary at root section.
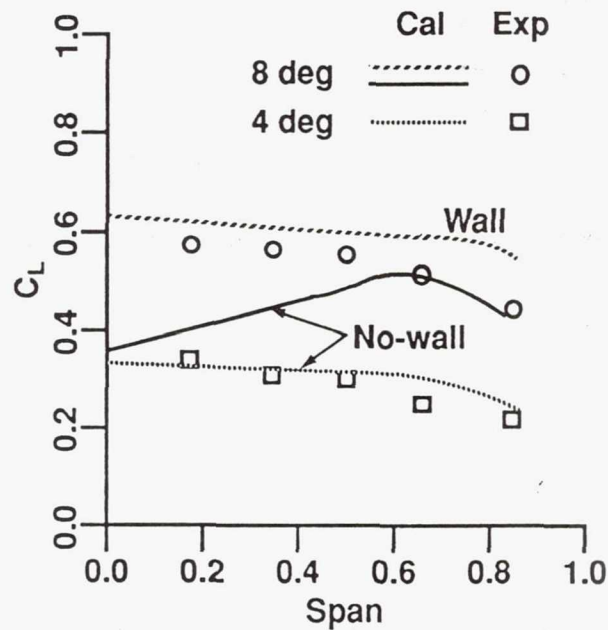
Fig. 8 Spanwise load distributions for the iced unswept wing at 4° and 8° angle of attack. No-wall and wall boundary conditions used.
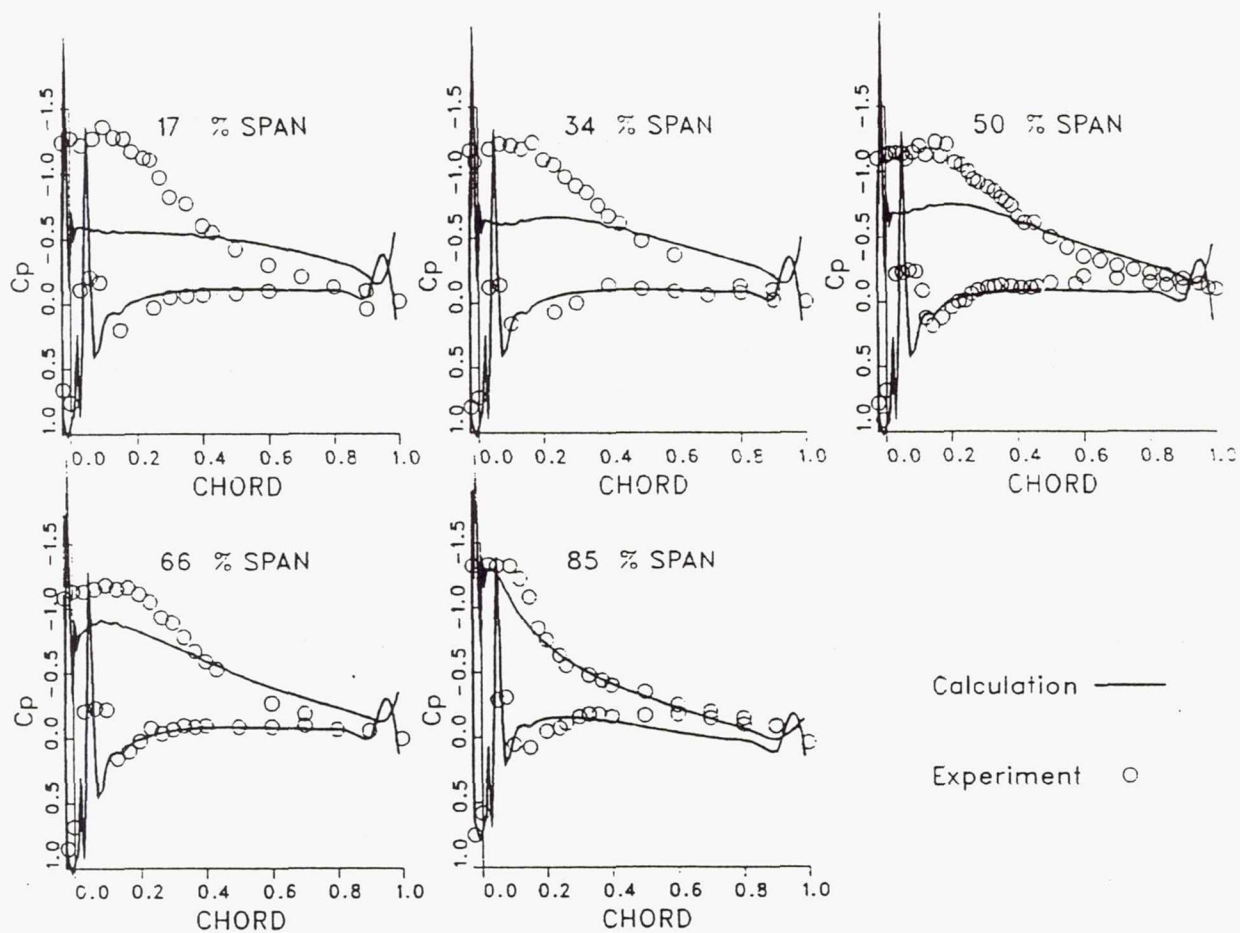
Fig. 9 Surface pressure distributions for the iced unswept wing at 8° angle of attack. No-wall boundary at root section.

Fig. 10 Surface pressure distributions for the iced unswept wing at 8° angle of attack. Wall boundary at root section.
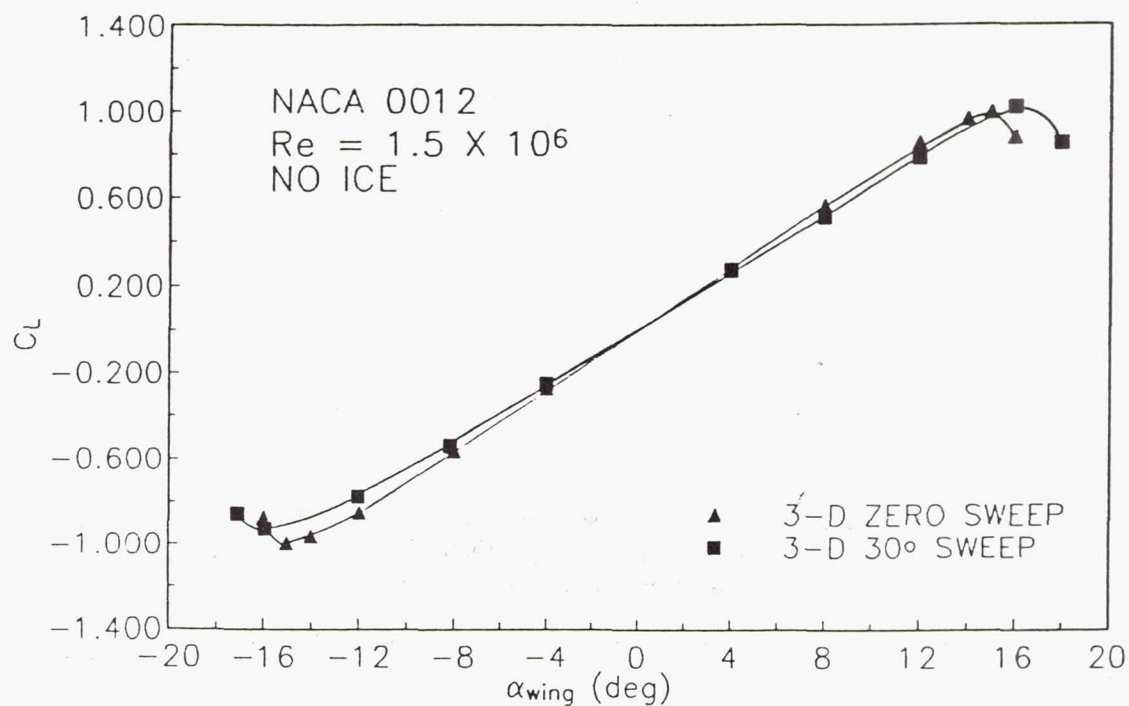

Fig. 11 3D lift performance of the swept wing compared to the unswept wing.

Fig. 12 Surface pressure distributions for the non-iced swept wing at 8° angle of attack. Wall and no-wall boundary at root section.

Fig. 13 Spanwise load distributions for the non-iced swept wing at 8° angle of attack. Wall and no-wall boundary at root section.

Fig. 14 Surface pressure distributions for the iced swept wing at 4° angle of attack. Wall boundary at root section.
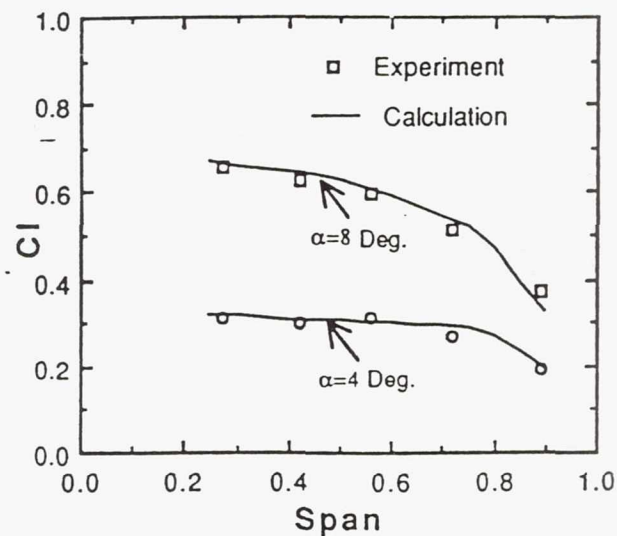
Fig. 15 Spanwise load distributions for the iced swept wing at 4° and 8° angle of attack.

14
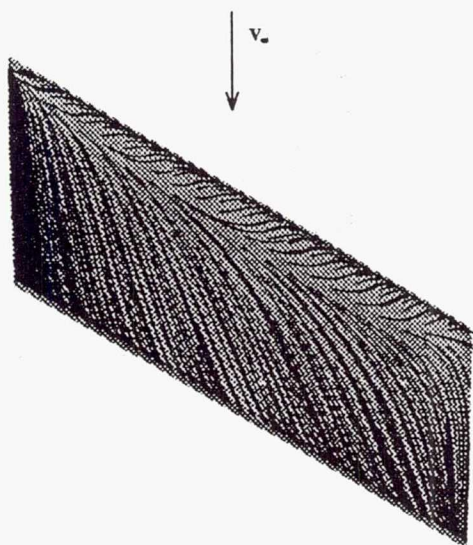
Fig. 16 Surface oil flow simulation for 30° swept
wing at 4° angle of attack.
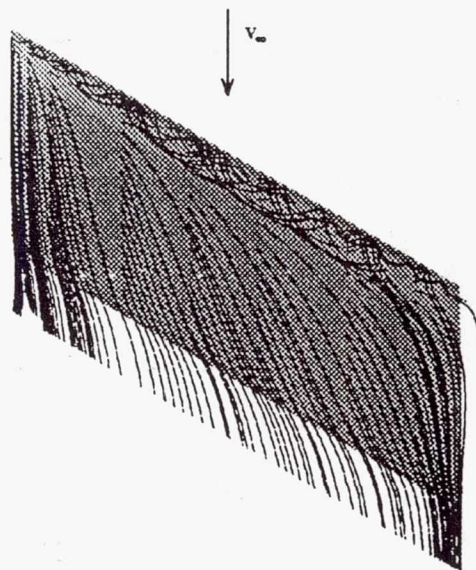
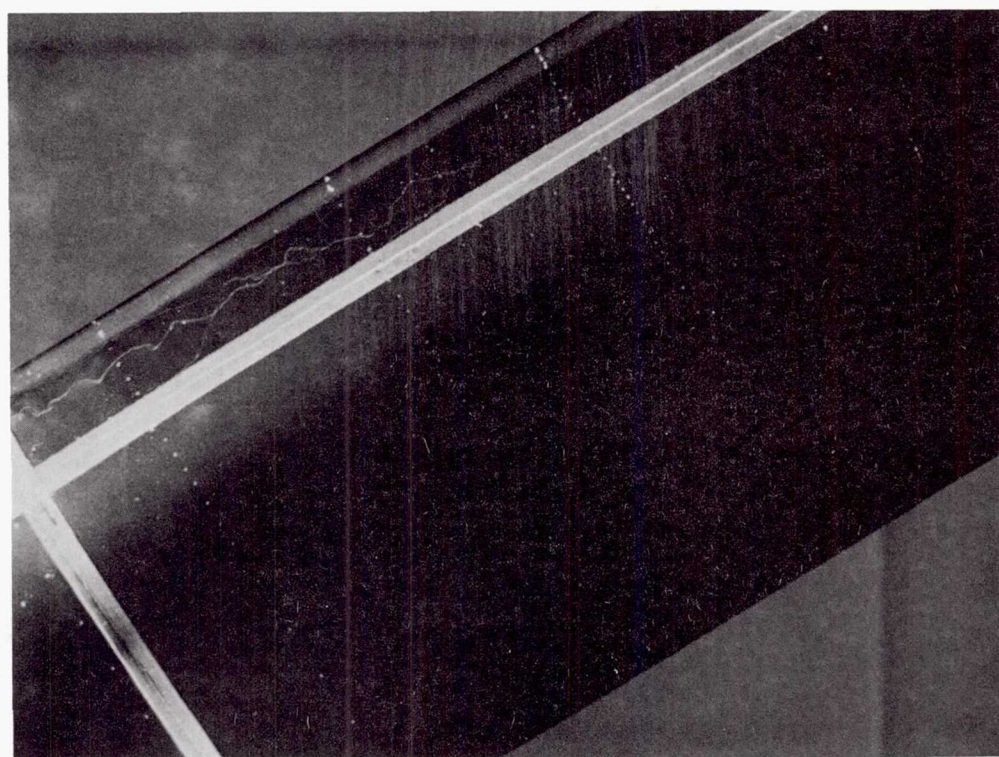Fig. 17 Off-body particle traces for 30° swept wing
at 4° angle of attack.

Fig. 18 Helium-bubble streaks over the upper surface of a swept wing with simulated glaze ice. Re = 6×10^5,
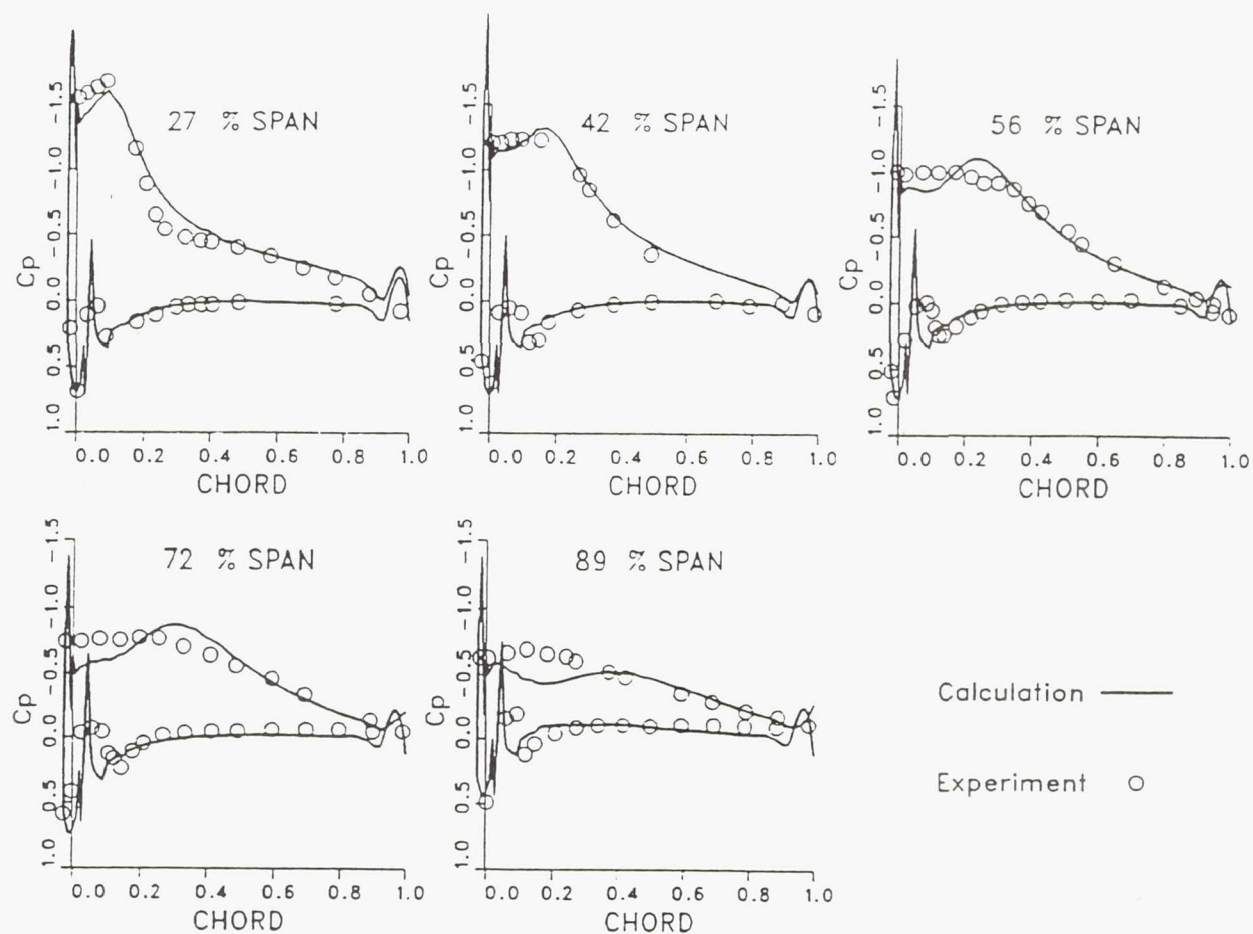$\alpha = 4°$.

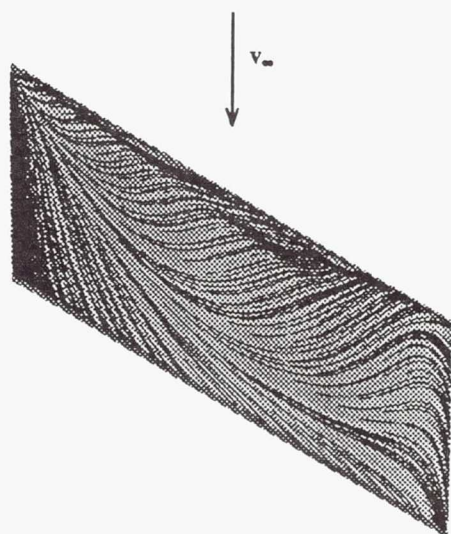Fig. 19 Surface pressure distributions for the iced swept wing at 8° angle of attack. Wall boundary at root section.

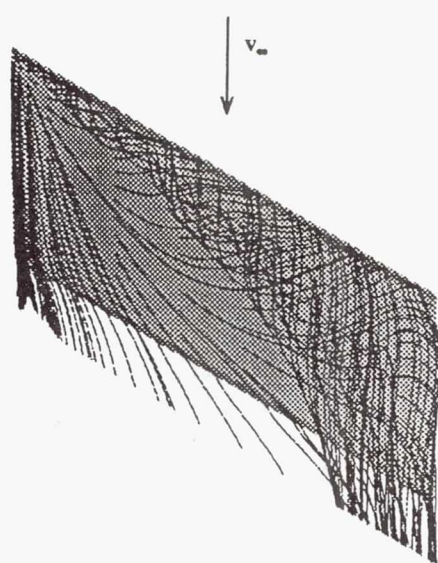Fig. 20 Surface oil flow simulation for 30° swept wing at 8° angle of attack.

Fig. 21 Off-body particle traces for 30° swept wing at 8° angle of attack.

1. Report No.	2. Government Accession No.	3. Recipient's Catalog No.
NASA TM -104362		

4. Title and Subtitle		5. Report Date
Simulation of Iced Wing Aerodynamics		
		6. Performing Organization Code

7. Author(s)	8. Performing Organization Report No.
M.G. Potapczuk, M.B. Bragg, O.J. Kwon, L.N. Sankar	E -6158
	10. Work Unit No.
	505-68-10

9. Performing Organization Name and Address	11. Contract or Grant No.
National Aeronautics and Space Administration Lewis Research Center Cleveland, Ohio 44135 - 3191	
	13. Type of Report and Period Covered

12. Sponsoring Agency Name and Address	Technical Memorandum
National Aeronautics and Space Administration Washington, D.C. 20546 - 0001	14. Sponsoring Agency Code

16. Abstract

The sectional and total aerodynamic load characteristics of moderate aspect ratio wings with and without simulated glaze leading-edge ice are studied both computationally, using a three-dimensional, compressible Navier-Stokes solver, and experimentally. The wing has an untwisted, untapered planform shape with NACA 0012 airfoil section. The wing has an unswept and swept configuration with aspect ratios of 4.06 and 5.0, respectively. Comparisons of computed surface pressures and sectional loads with experimental data for identical configurations are given. The abrupt decrease in the angle of attack for wing stall as a result of the leading edge ice formation is demonstrated numerically and experimentally.

17. Key Words (Suggested by Author(s))	18. Distribution Statement
Icing Aircraft hazards Aeronautics	Unclassified - Unlimited Subject Category 02

19. Security Classif. (of the report)	20. Security Classif. (of this page)	21. No. of pages	22. Price*
Unclassified	Unclassified	16	A03